

# Stochastic Liouville equations for hydrogen-bonding fluctuations and their signatures in two-dimensional vibrational spectroscopy of water

Thomas la Cour Jansen

*Institute for Theoretical Physics and Materials Science Centre, University of Groningen, Nijenborgh 4, 9747 AG Groningen, The Netherlands*

Tomoyuki Hayashi, Wei Zhuang, and Shaul Mukamel<sup>a)</sup>

*Department of Chemistry, University of California, Irvine, California 92697-2025*

(Received 26 April 2005; accepted 30 June 2005; published online 21 September 2005)

The effects of hydrogen-bond forming and breaking kinetics on the linear and coherent third-order infrared spectra of the OH stretch of HOD in D<sub>2</sub>O are described by Markovian, not necessarily Gaussian, fluctuations and simulated using the stochastic Liouville equations. Slow (0.5 ps) fluctuations are represented by a collective electrostatic coordinate, whereas fast (<100 fs) frequency fluctuations are described using either a second collective electrostatic coordinate or a four-state jump (FSJ) model for hydrogen-bonding configurations. Parameters for both models were obtained using a 1-ns molecular-dynamics trajectory calculated using the TIP4P force field combined with an electrostatic *ab initio* map. The asymmetry of the photon-echo spectra (larger linewidth on the blue side than on the red side) predicted by the FSJ is in better agreement with recent experiments. © 2005 American Institute of Physics. [DOI: 10.1063/1.2008251]

## I. INTRODUCTION

Liquid water has many unique properties, primarily due to its unusual capacity to form multiple hydrogen bonds. The nature of these bonds and their fluctuations has been the subject of extensive ongoing studies.<sup>1–45</sup>

The OH stretch vibrational spectrum of pure water is complicated by exciton transfer to neighboring molecules.<sup>10,12–16</sup> HOD in D<sub>2</sub>O is a simple model system where this transfer is not possible. Numerous infrared experiments have been performed on the OH stretch of the HOD/D<sub>2</sub>O system. The linear absorption spectrum<sup>17–19</sup> has a 255 cm<sup>-1</sup> bandwidth [full width at half maximum (FWHM)] and shows a 307 cm<sup>-1</sup> solvent redshift<sup>17</sup> from the gas phase frequency of 3707.47 cm<sup>-1</sup>.<sup>20</sup> Woutersen and Bakker<sup>21</sup> observed the vibrational Stokes shift in fluorescence to be 70 cm<sup>-1</sup>.<sup>22–25</sup> Vibrational relaxation and hydrogen-bond dynamics were also probed using spectral hole burning. Two-pulse photon-echo experiments and photon-echo peak shift were performed recently.<sup>18,19,26,27</sup> An oscillation in the peak shift was attributed to a coherent motion in the hydrogen bond,<sup>19</sup> in qualitative agreement with simulations.<sup>19,28</sup>

Similar experiments and simulations of the photon-echo technique on the complementary system (OD stretch of HOD in H<sub>2</sub>O) were reported as well.<sup>29,30</sup> The somewhat triangular shape of the two-dimensional peaks could not be reproduced by second-order cumulant expansion calculations and the time scales obtained from molecular-dynamics (MD) simulations were faster than observed in experiment. Of the three observed time scales the fastest (32 fs) was the same in the simulation and experiment. The intermediate time scale

(400 fs) was about 30% faster in the simulation (280 fs) while the slowest time scale observed was 1.8 ps and just 0.98 ps in the simulation.

Different approaches have been used to derive the fluctuating Hamiltonian required for simulating the nonlinear vibrational response. The first uses the MD force field directly to describe the solute-solvent interaction and employs an accurate Hamiltonian obtained from fit to experiment.<sup>15,31,32</sup> Subsequent treatments were based on the assumption that the electrostatic potential generated by the solvent is primarily responsible for the frequency changes in the solute. The frequency shift was then modeled as a quadratic Stark effect<sup>19</sup> or using an empirical fit to *ab initio* calculations of the fundamental frequency on clusters of a single solute surrounded by several solvent molecules.<sup>33,34</sup> We recently constructed a fluctuating Hamiltonian of HOD in D<sub>2</sub>O based on the diagonalized anharmonic *ab initio* vibrational Hamiltonian of the isolated solute in a spatially nonuniform electrostatic potential expanded around the center of charge.<sup>35</sup> A mapping between the electrostatic potential derivatives (the electric field and its gradient tensor) and the fluctuating frequencies of the solute was used to calculate the linear absorption.<sup>35</sup> The fluctuating Hamiltonian was obtained from MD trajectories by calculating the electric field and its gradient tensor on the HOD molecule. The linear response was calculated using four force fields and TIP4P and SPC were found to best reproduce the line shape and solvent shift. Unlike other maps, this map is not optimized to a particular solvent environment and is therefore transferable to other solvents. The field gradient tensor makes a considerable contribution to the frequency shift.<sup>35</sup> The map further provides a systematic way for identifying collective solvent coordinates that couple to the primary Hamiltonian, making it possible to incorporate general type of Markovian fluctuations (not necessarily

<sup>a)</sup>Electronic mail: smukamel@uci.edu

Gaussian) using the stochastic Liouville equation<sup>35–39</sup> (SLE) in the simulation of vibrational response functions.

Studies based on MD force fields combined with an accurate nonpolarizable solute Hamiltonian reproduced 64% of the experimental linewidth.<sup>15,40</sup> Both empirical *ab initio* maps<sup>33</sup> and the electrostatic *ab initio* map<sup>35</sup> reproduce the spectrum much better. The important role of solute polarization in the frequency calculations has been demonstrated.<sup>35</sup> Including the average polarization of the solvent was sufficient to reproduce the spectral linewidth. The two- and three-pulse photon-echo peak shift spectra simulated using a classical force field for the solute-solvent interaction<sup>28,41</sup> as well as by the linear Stark model<sup>19</sup> underestimate the size of the bump at 180 fs and the slow decay time scale. This difference was attributed to the force field.<sup>19,28</sup> The photon-echo spectrum of the OD stretch of HOD in H<sub>2</sub>O was simulated using the empirical *ab initio* map for the OD stretch.<sup>29</sup> The force fields underestimate the time scale for the slow decay of the frequency correlation function. The oscillation observed in the correlation function in earlier calculations<sup>41</sup> was also much less pronounced.

In this paper we first report the complete fluctuating Hamiltonian required for calculating the third-order response of the OH stretch of HOD in D<sub>2</sub>O based on our *ab initio* electrostatic map.<sup>35</sup> The electric field and its gradient were generated from classical MD simulations using the TIP4P force field. Two models were employed toward the simulation of the effects of hydrogen-bonding fluctuations on the line shapes. Both models describe the slow frequency fluctuations using a collective electrostatic coordinate (CEC) but differ in the treatment of the fast fluctuations. In the first, these are incorporated using an additional CEC, whereas the second is a discrete four-state jump (FSJ) model where the dynamics of four hydrogen-bonding configurations is described by kinetic equations for the breaking and forming of hydrogen bonds. In both models the OH stretch is coupled to a Markovian bath, and the optical response is simulated using the stochastic Liouville equation. For comparison the CEC line shapes were also calculated using the second-order cumulant and by a direct classical simulation. The CEC model gives rise to symmetric absorption line shapes, whereas the FSJ yields about 30% larger broadening on the blue side, in better agreement with experiment. The effect of the anharmonicity fluctuations on the nonlinear infrared spectra is investigated. The anharmonicity is found to be strongly correlated with the fundamental frequency and is significantly larger in the hydrogen-bonded red side of the spectrum.

Dissecting the spectra into different hydrogen-bonding configurations is not obvious, since these contributions strongly overlap.<sup>12,17,42</sup> Nevertheless, the model properly accounts for the non-Gaussian distribution of the OH band and its dynamics. A separation into different hydrogen-bonding species has been successfully used for the CO stretch of NMA in methanol.<sup>43</sup>

The electrostatic *ab initio* map and the MD simulations used to construct the fluctuating Hamiltonian are presented in Sec. II. The CEC model is described in Sec. III and the FSJ model is developed in Sec. IV. The connection between

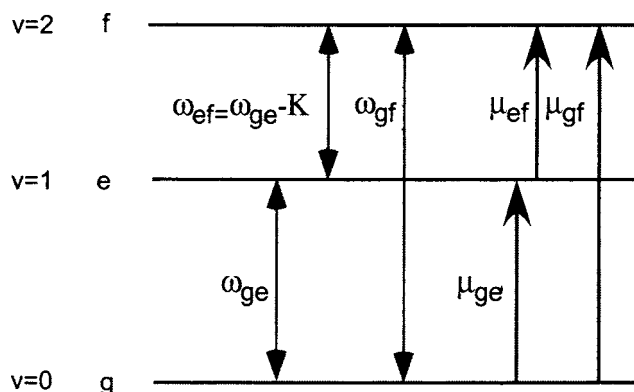


FIG. 1. Energy-level diagram for the OH stretch in HOD. The model has five vibrational parameters (two transition frequencies and three transition dipole moments) relevant for the infrared spectra.

hydrogen bonding and the fluctuating Hamiltonian, and the simulation protocol of the hydrogen-bonding motion are presented. The FSJ line shapes were simulated solely using the stochastic Liouville equation. The CEC line shapes were simulated using three techniques: CEC(i) uses the stochastic Liouville equation, CEC(ii) the second-order cumulant, and CEC(iii) classical simulation of phase fluctuations. The photon-echo spectra are presented in Sec. V. Finally, our results are discussed in Sec. VI.

## II. FLUCTUATING HAMILTONIAN FOR THE OH STRETCH

The fluctuating Hamiltonian for the OH stretch of HOD was obtained using the electrostatic *ab initio* map reported in Ref. 35. The map was constructed from the eigenstates calculation of the sixth-order anharmonic vibrational Hamiltonian of the HOD monomer by varying the external electric field and its gradient tensor. The anharmonic vibrational Hamiltonian in the presence of nonuniform external field was calculated with all three normal modes at the MP2/6-31+G(d,p) level using our modified GAUSSIAN03 code<sup>44</sup> (see Appendix A of Ref. 35). The map frequencies  $\omega$  and transition dipoles  $\mu$  were expanded to quadratic order in the electric field and its gradient tensor,

$$\omega_{g\nu} = \Omega_{\text{gas}}^{g\nu} + \sum_{\alpha} \Omega_{\alpha}^{g\nu} E_{\alpha} + \frac{1}{2} \sum_{\alpha\beta} \Omega_{\alpha\beta}^{g\nu} E_{\alpha} E_{\beta}, \quad (1)$$

$$\mu_{\nu\nu'} = M_{\text{gas}}^{\nu\nu'} + \sum_{\alpha} M_{\alpha}^{\nu\nu'} E_{\alpha} + \frac{1}{2} \sum_{\alpha\beta} M_{\alpha\beta}^{\nu\nu'} E_{\alpha} E_{\beta}.$$

Here  $\alpha$  and  $\beta$  denote the Cartesian components ( $x, y, z, xx, yy, zz, xy, xz, yz$ ) in the molecular coordinate system shown in Fig. 1(a) of Ref. 35.  $\nu$  and  $\nu'$  represent the ground state (g), the fundamental (e), and the first overtone (f) of the OH stretch, as shown in Fig. 1. The coefficients  $\Omega$  and  $M$  were given in Tables VII and VIII of Ref. 35. The electric field and its gradient were obtained from MD simulations with the TIP4P force field using the GROMACS package.<sup>45</sup> A 2.6 ns trajectory with 4 fs sample points was calculated at 300 K, 1 bar *NPT* ensemble<sup>46</sup> with 215 D<sub>2</sub>O molecules and one HOD.<sup>35</sup> The frequencies and dipole mo-

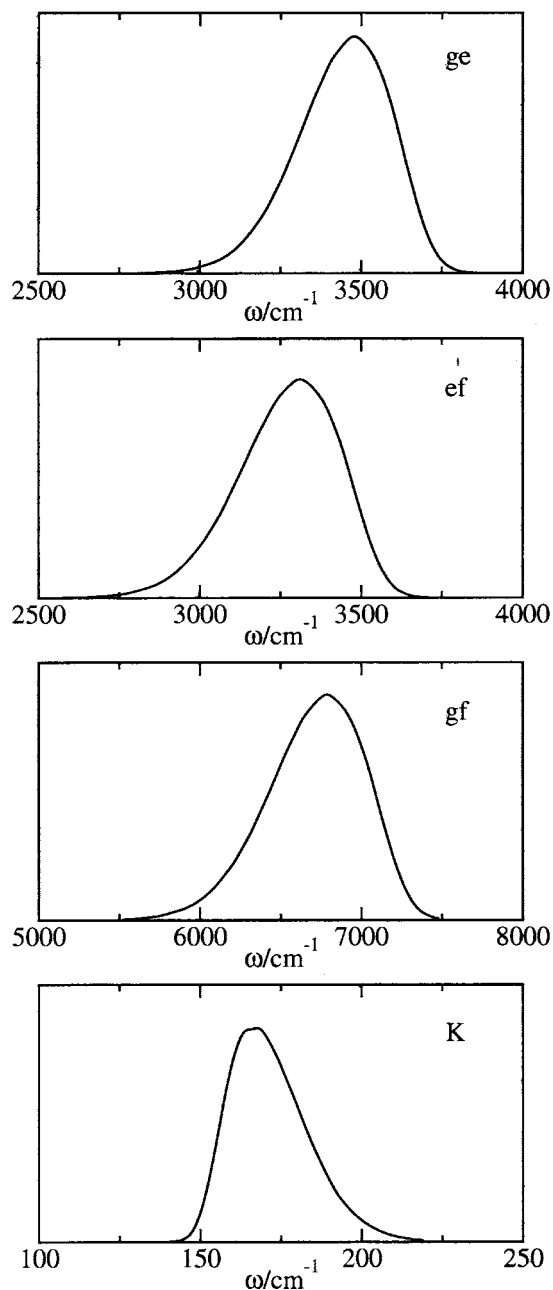


FIG. 2. Static distribution of the OH stretch transition frequencies ( $ge$ ,  $ef$ , and  $gf$ ) and anharmonicity ( $K \equiv 2\omega_{ge} - \omega_{gf}$ ).

ments of the three lowest OH stretch vibrational states (Fig. 1) were obtained by combining the *ab initio* map with electric-field trajectories.

The distributions and correlation functions of the fundamental frequency  $\omega_{ge}$  and its transition dipole  $\mu_{ge}$  were reported in Ref. 35. In Fig. 2 we display the distributions of all frequencies  $\omega_{ge}$ ,  $\omega_{gf}$ ,  $\omega_{ef}$  and the anharmonicity  $K \equiv 2\omega_{ge} - \omega_{gf}$ . The statistics is reported in Table I. The time correlation functions calculated using the harmonic quantum correction<sup>35,47</sup> are shown in Fig. 3.

The calculated average anharmonicity ( $\langle K \rangle = 2\langle \omega_{ge} \rangle - \langle \omega_{gf} \rangle$ ) is  $171.9 \text{ cm}^{-1}$  and its variance  $\sigma$  is  $12.41 \text{ cm}^{-1}$ . An anharmonicity of  $182 \text{ cm}^{-1}$  was reported by other calculations.<sup>41</sup> Pump-probe spectra gave an anharmonic shift of  $270 \pm 20 \text{ cm}^{-1}$ ,<sup>21,22</sup> while hole-burning gave  $240 \pm 20 \text{ cm}^{-1}$ .<sup>48</sup>

TABLE I. Statistical data for the fluctuating frequencies for the considered transitions.

Transition	$ge$	$ef$	$gf$
$\langle \omega \rangle (\text{cm}^{-1})$	3439.0	3267.2	6706.2
$\sigma (\text{cm}^{-1})$	146.8	158.6	305.4

The average transition dipole  $\langle \mu_{ge} \rangle$  is 9.50 D,  $\langle \mu_{ef} \rangle$  is 13.00 D, and  $\langle \mu_{gf} \rangle$  is 1.00 D. The ratio  $\langle \mu_{ef} \rangle / \langle \mu_{ge} \rangle = 1.369$  (for a harmonic mode it is  $\sqrt{2} = 1.414$ ). These fluctuations are much smaller than the average dipole moments and were neglected. The variances of the fluctuations are 1.7 D ( $\mu_{ge}$ ), 3.7 D ( $\mu_{ef}$ ), and 0.28 D ( $\mu_{gf}$ ).<sup>35</sup> The scatter plot in Fig. 4 shows that the overtone frequency and the anharmonicity are highly correlated with the fundamental frequency. We also found the transition dipoles to be highly correlated.

### III. THE COLLECTIVE ELECTROSTATIC COORDINATE (CEC) MODEL

The nonlinear response of a quantum multilevel system coupled to a stochastic bath can be simulated using the SLE,<sup>36,37,49</sup> which describes their joint time evolution,

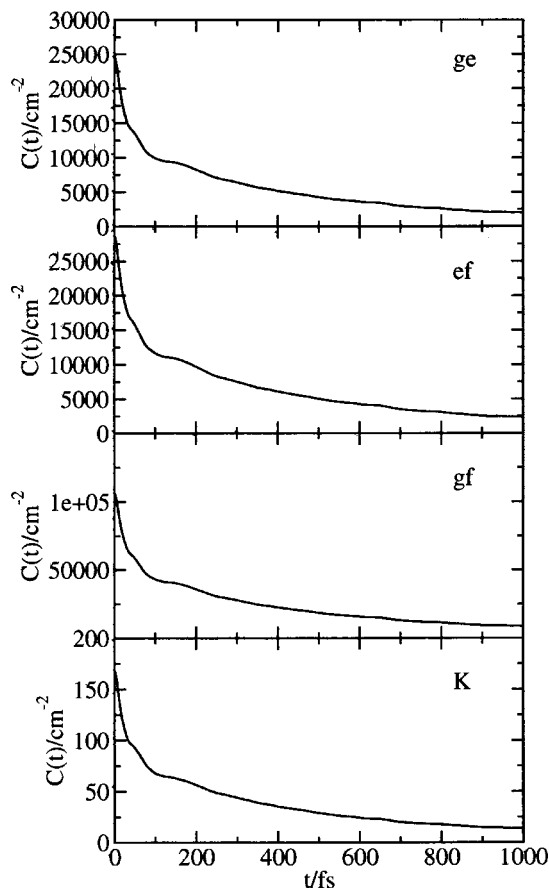


FIG. 3. Autocorrelation functions of the transition frequencies ( $ge$ ,  $ef$ , and  $gf$ ) and the anharmonicity ( $K$ ).

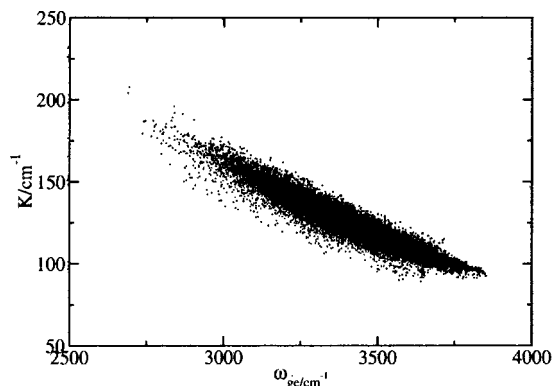


FIG. 4. Scatter plot showing the correlation between the anharmonicity  $K$  and the fundamental frequency  $\omega_{ge}$ .

$$\begin{aligned} \dot{\rho}(\mathbf{\Omega}, t) = & -\frac{i}{\hbar}[H_0(\mathbf{\Omega}), \rho(\mathbf{\Omega}, t)] + \sum_{i=1}^2 \Gamma_i \rho(\mathbf{\Omega}, t) \\ & + \frac{i}{\hbar}[\varepsilon(t)\mu, \rho(\mathbf{\Omega}, t)], \end{aligned} \quad (2)$$

where  $\rho$  is the density matrix of the multilevel system which depends parametrically on the collective bath coordinates  $\mathbf{\Omega}$ . In our case  $\rho$  is the  $3 \times 3$  density matrix of the lowest three states of the OH stretch ( $g$ ,  $e$ , and  $f$ ).  $H_0$  only acts on the system space of  $\rho$  and is a diagonal matrix with diagonal elements 0,  $\omega_{ge}(\mathbf{\Omega})$ , and  $\omega_{gf}(\mathbf{\Omega}) = \omega_{ge}(\mathbf{\Omega}) + \omega_{ef}(\mathbf{\Omega})$ . We define the anharmonicity as  $K(\mathbf{\Omega}) \equiv 2\omega_{ge}(\mathbf{\Omega}) - \omega_{gf}(\mathbf{\Omega})$ . The frequency fluctuations can be expressed in terms of a single collective coordinate  $\mathbf{\Omega}$ , which is a linear combination of the nine independent components of fluctuating electric field and its gradients.<sup>35</sup> This coordinate has a biexponential correlation function. To obtain a Markovian description we have decomposed it into a sum of a fast ( $\Omega_1$ ) and a slow ( $\Omega_2$ ) Brownian oscillator coordinates  $\mathbf{\Omega} = \Omega_1 + \Omega_2$ .<sup>35</sup>

$$\omega_{ge}(\mathbf{\Omega}) = 3450.6 + \Omega_1 + \Omega_2 - 0.000554(\Omega_1 + \Omega_2)^2, \quad (3)$$

$$K(\mathbf{\Omega}) = 171.8 - 0.0800(\Omega_1 + \Omega_2) + 0.000063(\Omega_1 + \Omega_2)^2, \quad (4)$$

where  $\omega_{ge}$ ,  $K$ , and  $\mathbf{\Omega}$  are in  $\text{cm}^{-1}$ . The time evolution of the joint distribution  $P(\mathbf{\Omega})$  of  $\Omega_1$  and  $\Omega_2$  is described by the Smoluchowski equation for two independent Brownian oscillators,

$$\frac{dP(\mathbf{\Omega}, t)}{dt} = \sum_{i=1}^2 \Gamma_i P(\mathbf{\Omega}, t), \quad (5)$$

where

$$\Gamma_i \equiv \frac{1}{\tau_i} \frac{\partial}{\partial \Omega_i} \left( \Omega_i + \sigma_i^2 \frac{\partial}{\partial \Omega_i} \right). \quad (6)$$

The relaxation times for  $\Omega_1$  and  $\Omega_2$  are  $\tau_1 = 0.501$  ps and  $\tau_2 = 34.4$  fs. The widths of the equilibrium distribution  $\sigma_i$  for  $\Omega_1$  and  $\Omega_2$  are  $\sigma_1 = 110.1$   $\text{cm}^{-1}$  and  $\sigma_2 = 104.4$   $\text{cm}^{-1}$ . The correlation functions are  $\langle \Omega_i(t) \Omega_j(0) \rangle = \delta_{ij} \sigma_i^2 \exp(-t/\tau_i)$  yielding an overall biexponential correlation function of the collective electrostatic coordinate  $\langle \mathbf{\Omega}(t) \mathbf{\Omega}(0) \rangle = \sigma_1^2 \exp(-t/\tau_1)$

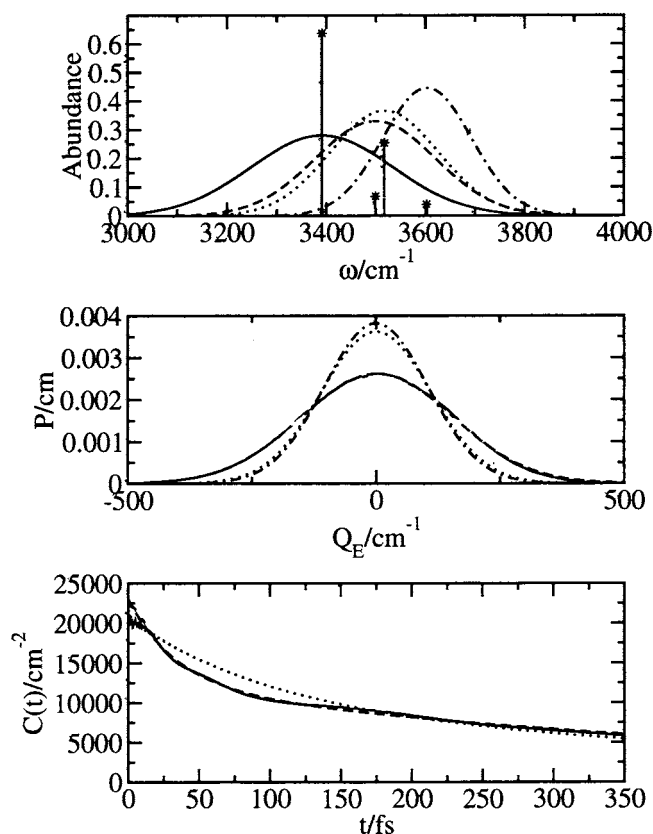


FIG. 5. Upper panel: The vertical lines marked with stars show the center position of the four states of the FSJ model. The height of each line marks the probability of the state. The Gaussian lines on top illustrate the slowly changing frequency distribution added on top of each state (solid: I, dotted: II, dashed: III, and dash-dotted: IV). Middle panel: The solid line is the distribution of the collective electrostatic coordinate. The dashed line on top is the Gaussian distribution corresponding to the combination of the Gaussian distributions of the coordinates  $\Omega_1$  and  $\Omega_2$ . The distributions of these coordinates are the dotted and dash-dotted lines, respectively. Lower panel: solid line: The correlation function of the collective electrostatic coordinate; dashed line: the biexponential fit. The dotted line is the FSJ frequency correlation function.

$+ \sigma_2^2 \exp(-t/\tau_2)$ . These time scales are comparable to those suggested by the first biexponential model (50 and 800 fs) for the frequency correlation function.<sup>50</sup> The correlation function and the biexponential fit are shown in Fig. 5.

The last term in Eq. (2) represents the coupling of the OH stretch to the optical electric field  $\varepsilon$ , and  $\mu$  is the transition dipole moment matrix of an isolated HOD molecule,

$$\mu = \begin{pmatrix} 0 & M^{ge} & M^{gf} \\ M^{ge} & 0 & M^{ef} \\ M^{gf} & M^{ef} & 0 \end{pmatrix}. \quad (7)$$

The optical field couples to the OH stretch, but not to the bath coordinates.

The response function was calculated directly in the frequency domain by solving the SLE. The Green's functions describing the time evolution in the joint space of the OH stretch and the collective coordinates were calculated using a matrix-continued fraction. The expressions for the third-order response were given in Appendix B of Ref. 49. We shall denote the calculation based on Eq. (2) as CEC(i). We have further solved the same model using two other tech-

TABLE II. Number of hydrogen bonds to each atom (H, D, and O), average frequency ( $\langle\omega_{ge}\rangle$ ), frequency spread ( $\sigma_{ge}$ ), and abundance ( $P$ ) for the hydrogen-bonding configurations.

Group	Conf.	H	D	O	$\langle\omega_{ge}\rangle(\text{cm}^{-1})$	$\sigma_{ge}(\text{cm}^{-1})$	$P$ (%)
I	0	1	0	2	3382.6	142.1	6.4
	1	1	1	2	3392.2	142.1	57.4
II	2	1	0	1	3505.8	108.9	3.3
	3	1	1	1	3515.7	109.5	21.1
	4	1	0	0	3576.4	71.8	0.2
	5	1	1	0	3578.3	71.7	0.9
III	6	0	0	2	3483.9	119.4	0.6
	7	0	1	2	3500.5	120.9	6.2
IV	8	0	0	1	3584.6	89.5	0.5
	9	0	1	1	3604.1	90.4	3.3
	10	0	0	0	3627.4	58.7	0.0
	11	0	1	0	3640.6	50.9	0.2

niques. CEC(ii) describes the frequency fluctuations using the second-order cumulant expansion.<sup>35,51,52</sup> This approximation assumes that the frequencies are linearly coupled to a Gaussian process [i.e., we neglect the quadratic terms in Eqs. (3) and (4)] and does not require to identify Markovian coordinates. CEC(iii) is a direct averaging of classical phase fluctuations as described in Appendix D of Ref. 49.

#### IV. THE FOUR-STATE JUMP-MODEL FOR FAST HYDROGEN-BOND FLUCTUATIONS

The FSJ simulation connects the contributions of fast fluctuations to the infrared line shapes directly with stochastic transitions between different hydrogen-bonding configurations. The 12 hydrogen-bonded configurations were examined by employing the geometric hydrogen-bonding criteria<sup>9,53,54</sup> requiring the O–O distance to be less than 3.5 Å and the OOH angle to be less than 30° for a pair of water molecules to be characterized as hydrogen bound. Hydrogen and deuterium can both donate one hydrogen bond, while oxygen can accept two. The geometric criteria occasionally give rise to more hydrogen bonds than this. If more than one hydrogen bond to hydrogen is found, only the shortest is characterized as a hydrogen bond and if more than two hydrogen bonds are found to oxygen only the two shortest are accepted. The hydrogen-bonding patterns obtained from the simulation described in Sec. II for the 12 configurations along with the abundance are listed in Table II. We further give the average OH fundamental frequency and its variance

calculated using our electrostatic model. The OH stretch is redshifted by hydrogen bonding.<sup>4</sup> We found that hydrogen bonding to hydrogen gives a 100 cm<sup>-1</sup> redshift. The first hydrogen bond to oxygen redshifts the frequency by between 30 and 40 cm<sup>-1</sup> while the second hydrogen bond redshifts the frequency by 100–120 cm<sup>-1</sup>.

Since only a few of the configurations have significant populations, we have clustered the 12 configurations into four groups, as given in Table II, configuration I (1 hydrogen bond to hydrogen and 2 to oxygen), II (1 hydrogen bond to hydrogen and less than 2 to oxygen), III (no hydrogen bond to hydrogen, but 2 hydrogen bonds to oxygen), and IV (no hydrogen bonds to hydrogen and has less than 2 hydrogen bonds to oxygen). Hydrogen bonding to deuterium atom blueshifts the frequency by 10–20 cm<sup>-1</sup>. This small effect was neglected in this clustering. It is not possible to define from the simulations an exact boundary between hydrogen-bonded and free systems.<sup>9,54,55</sup> A broad distribution of hydrogen bonds with different strength exists, and it is somewhat arbitrary whether a weak hydrogen-bond configuration is taken to be a bond; the choice of the hydrogen-bonding criteria affects the populations and relaxation rates. The statistics for these four configurations is given in Table III. The average fundamental frequency  $\langle\omega_{ge}\rangle$ , average overtone frequency  $\langle\omega_{ef}\rangle$ , and average anharmonicity  $\langle K\rangle$  were obtained from the MD trajectories. We also present the variances  $\sigma = \sqrt{\langle\omega^2\rangle - \langle\omega\rangle^2}$  of the fundamental frequency fluctuations  $\sigma_{ge}$  and the overtone frequency fluctuations  $\sigma_{ef}$ . The lifetime of each configuration was calculated by fitting the lifetime histograms as described later in this section. The population  $P$  of each configuration was obtained by binning the snapshots into various configurations. Configuration I dominates with 63.3% of the population and configuration II, where one of the hydrogen bonds on oxygen is broken, accounts for most of the remaining population. The redshift and the frequency variance are the largest in I and the smallest in IV. The overtone frequency is influenced by the hydrogen bonding in a similar way to the fundamental.  $\omega_{ef}$  is reported in Table III along with the spread in this frequency and the anharmonicity. The frequency redshift as well as the frequency spread and anharmonicity is the largest in I and smallest in IV following the trend found for the fundamental. The frequency distributions of the four configurations are given in Fig. 6.

The four configurations interconvert by breaking and forming of hydrogen bonds. We assumed the kinetic scheme depicted in Fig. 7, where only one hydrogen bond is broken or formed at a time. This leads to four reactions labeled A–D, where A and C involve the hydrogen bond on oxygen and B and D the hydrogen bond on hydrogen.

TABLE III. Frequencies ( $\langle\omega_{ge}\rangle$  and  $\langle\omega_{ef}\rangle$ ), frequency distributions ( $\sigma_{ge}$  and  $\sigma_{ef}$ ), anharmonicity ( $K$ ) dependence on the hydrogen-bond configuration, lifetime  $\tau$ , and abundance ( $P$ ).

Conf.	$\langle\omega_{ge}\rangle(\text{cm}^{-1})$	$\sigma_{ge}(\text{cm}^{-1})$	$\langle\omega_{ef}\rangle(\text{cm}^{-1})$	$\sigma_{ef}(\text{cm}^{-1})$	$\langle K\rangle(\text{cm}^{-1})$	$\tau(\text{fs})$	$P$ (%)
I	3391.2	142.2	3215.3	153.8	176.0	65.3	63.8
II	3517.0	108.9	3352.3	116.8	164.7	36.3	25.4
III	3499.0	120.8	3331.2	130.1	167.8	17.1	6.8
IV	3603.2	89.4	3444.0	95.3	159.2	16.5	4.0

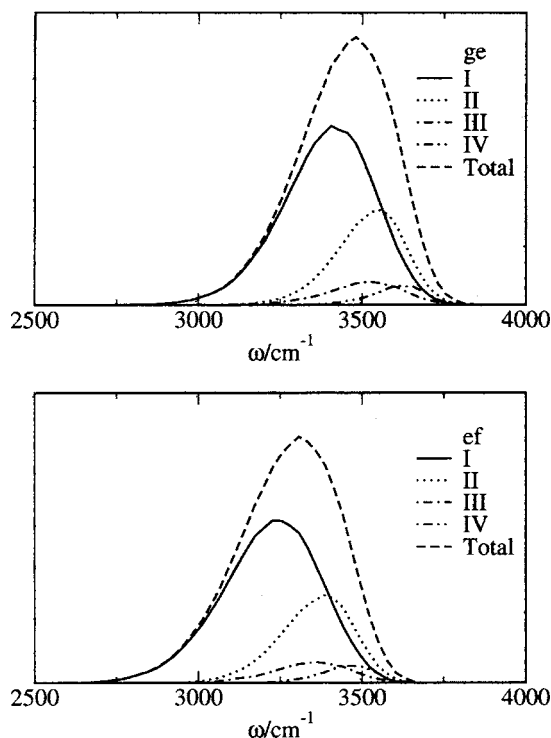


FIG. 6. Distribution of the fundamental and overtone frequencies for the four hydrogen-bond species. I: solid, II: dotted, III: dash-dotted, IV: dash-dot-dotted, and total: dashed line. The integrated intensity of each curve gives the abundance of each species.

The residence time in a given configuration was calculated from the MD trajectory, and lifetime histograms were constructed for each of the four configurations. The lifetimes of the four configurations given in Table III were then determined by exponential fits of the lifetime histograms (see Fig. 8). Configurations I and II have much longer lifetimes than III and IV. The equilibrium constants for the four hydrogen-bond breaking reactions obtained from the equilibrium populations are given in Table IV. Each configuration has two possible reactions (Fig. 7). For each reaction the equilibrium constant  $\mathcal{K}$  determine the ratio between the reaction constants for hydrogen-bond breaking ( $k^b$ ) and forming ( $k^f$ ) by the detailed balanced conditions,  $\mathcal{K}_A = k_A^b/k_A^f = P(\text{II})/P(\text{I})$ ,  $\mathcal{K}_B = k_B^b/k_B^f = P(\text{III})/P(\text{I})$ ,  $\mathcal{K}_C = k_C^b/k_C^f = P(\text{IV})/P(\text{III})$ , and  $\mathcal{K}_D = k_D^b/k_D^f = P(\text{IV})/P(\text{II})$ . The lifetime ( $T$ ) of each configuration was determined by the rate constants for the reactions that lead away from that configuration,  $1/T_I = k_A^b + k_B^b$ ,  $1/T_{II} = k_A^f + k_D^b$ ,  $1/T_{III} = k_B^f + k_C^b$ , and  $1/T_{IV} = k_D^f + k_C^f$ . The equilibrium

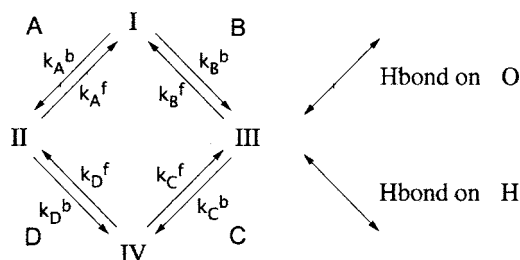


FIG. 7. Kinetic scheme for the four hydrogen-bonding configurations. Reactions A and C break<sup>b</sup>/form<sup>f</sup> hydrogen bonds on oxygen, while B and D break<sup>b</sup>/form<sup>f</sup> hydrogen bonds on hydrogen.

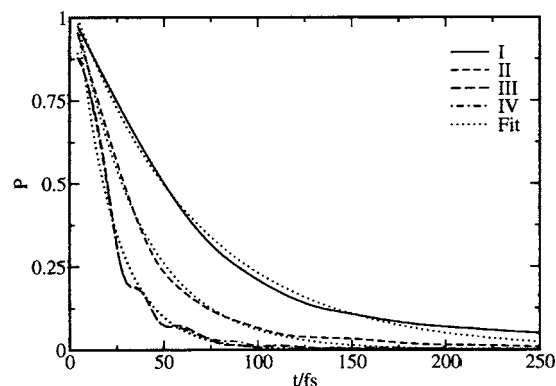


FIG. 8. Lifetime histograms for the four hydrogen-bond configurations.  $P$  is the probability that the configuration survives a specified time. Solid line: configuration I, small dashed line: II, large dashed line: III, and dash-dotted: IV. The dashed lines are fitted exponential decays.

constants  $\mathcal{K}_A$ ,  $\mathcal{K}_B$ ,  $\mathcal{K}_C$ , and  $\mathcal{K}_D$  were obtained from the populations reported in Table III using the detailed balance relations. The lifetimes  $T_I$ ,  $T_{II}$ ,  $T_{III}$ , and  $T_{IV}$  were found by the lifetime histograms described above. The rate constants  $k$  computed from  $\mathcal{K}$  and  $T$  are listed in Table IV.

In the FSJ model,  $\Omega_2$  in Eq. (6) is replaced by a kinetic equation describing the stochastic jumps among the four states described above:

$$\frac{d}{dt} \begin{pmatrix} P(\text{I}) \\ P(\text{II}) \\ P(\text{III}) \\ P(\text{IV}) \end{pmatrix} = \begin{bmatrix} -k_A^b - k_B^b & k_A^f & k_B^f & 0 \\ k_A^b & -k_A^f - k_D^b & 0 & k_D^f \\ k_B^b & 0 & -k_B^f - k_C^b & k_C^f \\ 0 & k_D^b & k_C^b & -k_C^f - k_D^f \end{bmatrix} \times \begin{pmatrix} P(\text{I}) \\ P(\text{II}) \\ P(\text{III}) \\ P(\text{IV}) \end{pmatrix}. \quad (8)$$

We represent this equation as  $\dot{P} = \Gamma_J P$ .  $\Gamma_J$  is the relaxation operator describing the jumps between the four hydrogen-bond configurations given by the  $4 \times 4$  matrix in the rate equation [Eq. (8)]. Within each state an additional continuous broadening due to slow bath coordinates  $\Omega_1$  is added. The relaxation time  $\tau_1$  from the CEC(i) model was then used for this broadening and the  $\sigma_1$  was taken from the spread in the individual configurations given in Table III.

TABLE IV. Reaction dynamics for hydrogen-bond breaking and forming.

Reaction	A	B	C	D
Eq. const. $\mathcal{K}$	0.398	0.106	0.597	0.159
Breaking [ $k^b$ (ps <sup>-1</sup> )]	14.7	4.4	14.6	5.8
Forming [ $k^f$ (ps <sup>-1</sup> )]	36.8	41.4	24.4	36.3

Each density-matrix element  $\rho_{\nu\nu'}$  becomes a four-dimensional vector with components representing the hydrogen-bonding configurations I, II, III, and IV, which further depends on the coordinate  $\Omega_1$ . The final SLE for the FSJ model is

$$\dot{\rho}(\Omega_1, t) = -\frac{i}{\hbar}[H(\Omega_1), \rho(\Omega_1, t)] - \Gamma_1 \rho(\Omega_1, t) - \Gamma_1(\Omega_1) \rho(\Omega_1, t) + \frac{i}{\hbar}[\varepsilon(t)\mu, \rho(\Omega_1, t)]. \quad (9)$$

The Hamiltonian block  $H^q(\Omega_1)$  for each hydrogen-bond species ( $q=I-IV$ ) in Table III is a  $3 \times 3$  diagonal matrix elements 0,  $\omega_{ge}^q(\Omega_1)$ , and  $\omega_{gf}^q(\Omega_1) = \omega_{ge}^q(\Omega_1) + \omega_{ef}^q(\Omega_1)$ . The frequencies for the four configurations (I–IV) are

$$\omega_{ge}^q(\Omega_1) = \langle \omega_{ge}^q \rangle + r_{gc}^q \Omega_1, \quad (10)$$

$$\omega_{gf}^q(\Omega_1) = \langle \omega_{gf}^q \rangle + r_{ef}^q \Omega_1,$$

where  $r^q$  is the ratio  $\sigma_q/\sigma_1$  between the distribution of the frequencies within one configuration (Table III) and the overall distribution of the slow coordinate described in Sec. III. The weak quadratic dependence of the frequencies on the slow collective coordinate  $\Omega_1$  was neglected.  $\Gamma_1$  is a relaxation operator for the slow collective coordinate  $\Omega_1$  [Eq. (6)].

In FSJ the hydrogen-bonding kinetics replaces the fast collective coordinate ( $\Omega_2$ ) in CEC. The time evolution of the density-matrix block  $\rho_{\nu\nu'}$  ( $\nu\nu'$  are either  $ge$ ,  $eg$ , or  $fe$ ) due to the first and the second terms on the right-hand side of Eq. (9) is given by combining Eqs. (8)–(10),

$$\begin{pmatrix} \dot{\rho}_{\nu\nu'}^{I} \\ \dot{\rho}_{\nu\nu'}^{II} \\ \dot{\rho}_{\nu\nu'}^{III} \\ \dot{\rho}_{\nu\nu'}^{IV} \end{pmatrix} = \begin{pmatrix} -\frac{i}{\hbar}(\omega_{\nu\nu'}^I + r_{\nu\nu'}^I \Omega_1) & k_A^f & k_B^f & 0 \\ -k_A^b - k_B^b & & & \\ k_A^b & -\frac{i}{\hbar}(\omega_{\nu\nu'}^{II} + r_{\nu\nu'}^{II} \Omega_1) & 0 & k_D^f \\ -k_A^f - k_D^b & & & \\ k_B^b & 0 & -\frac{i}{\hbar}(\omega_{\nu\nu'}^{III} + r_{\nu\nu'}^{III} \Omega_1) & k_C^f \\ -k_B^f - k_C^b & & & \\ 0 & k_D^b & k_C^b & -\frac{i}{\hbar}(\omega_{\nu\nu'}^{IV} + r_{\nu\nu'}^{IV} \Omega_1) \\ & & & -k_C^f - k_D^f \end{pmatrix} \begin{pmatrix} \rho_{\nu\nu'}^{I} \\ \rho_{\nu\nu'}^{II} \\ \rho_{\nu\nu'}^{III} \\ \rho_{\nu\nu'}^{IV} \end{pmatrix}. \quad (11)$$

The third term in Eq. (9) acts only in the  $\Omega_1$  space and the fourth term only in the system space.

The FSJ assumes that the system makes sudden jumps between the different hydrogen-bond configurations, while in the CEC these configurational changes are a continuous process where hydrogen-bonding dynamics is not treated explicitly but is represented by the collective coordinate. The frequency correlation function of the FSJ model is shown in Fig. 5 along with the correlation function of the electrostatic coordinate, the positions, and population of the four states and the slowly varying distribution of frequencies.

## V. THE PHOTON-ECHO SPECTRA

The photon-echo spectra were calculated for the FSJ and CEC models. The photon echo is a sum of three Liouville space pathways given in Fig. 9. The Green function solution of the SLE was given in Eqs. (B13)–(B16) of Ref. 49. The procedure for incorporating the pulse bandwidth within the rotating wave approximation by selecting the resonant transitions was outlined in Ref. 56 for rectangular pulses. In the present simulation we assumed Gaussian pulses with a cen-

tral frequency of  $3450 \text{ cm}^{-1}$  and a width of  $120 \text{ cm}^{-1}$  corresponding to a pulse duration of 45 fs using Eq. (A8) of Ref. 57.

The linear infrared line shapes for the CEC(i) and FSJ models shown in Fig. 10 are very similar and reproduce the experimental line shape. Both line shapes have the longer red tail reflecting the asymmetric static distribution (Fig. 2).

The photon-echo spectra displayed in Fig. 11 were calculated using Eqs. (B13)–(B16) of Ref. 49 with the Greens functions obtained from the matrix-continued fraction representation as described in Appendix E of the same reference using Eq. (9). The antidiagonal cuts through the diagonal peak are shown in Fig. 12. The antidiagonal linewidth in CEC(i) is about the same at the low and the high frequency while for the FSJ the linewidth is higher for higher frequencies. The blue lines are clearly broader than the red lines for the FSJ. The FWHM of the peaks are given in Table V. The width in the low-frequency region is about the same for all models. The CEC(i) width is about  $2 \text{ cm}^{-1}$  broader in the blue than in the red while the FSJ is about 30% ( $23 \text{ cm}^{-1}$ ) broader in the blue. This is despite the fact that the distribution of frequencies as given in Table III is broader for the

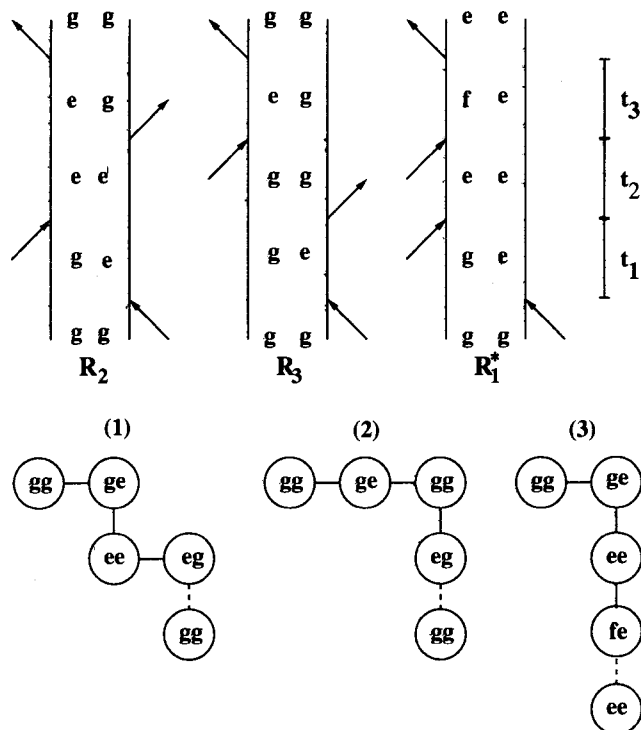


FIG. 9. The three Liouville space pathways contributing to the photon-echo signal.  $R_2$  represents stimulated emission,  $R_3$  represents ground-state bleach, and  $R_1^*$  shows excited-state absorption.

low-frequency configuration I. We define the asymmetry parameter  $\eta$  as the FWHM in the red and the blue of the anti-diagonal sections of Fig. 12,

$$\eta = \frac{\text{FWHM}(\text{blue}) - \text{FWHM}(\text{red})}{\text{FWHM}(\text{blue}) + \text{FWHM}(\text{red})}, \quad (12)$$

where  $\eta$  is 0.0138 for the CEC(i) and 0.125 for the FSJ using the FWHM values in Table V. The experimental  $\eta$  is 0.0848 closer to the FSJ value, suggesting that the short lifetime of the high-frequency hydrogen-bond species gives rise to a considerable line broadening.<sup>58</sup> The hydrogen-bond kinetics must be much faster than the slow dynamics giving rise to the frequency distribution of the individual species.

Hole-burning spectroscopy shows different linewidths<sup>48</sup> for the low- and the high-frequency species (70 and 90  $\text{cm}^{-1}$ , respectively). These and similar observations for HOD in

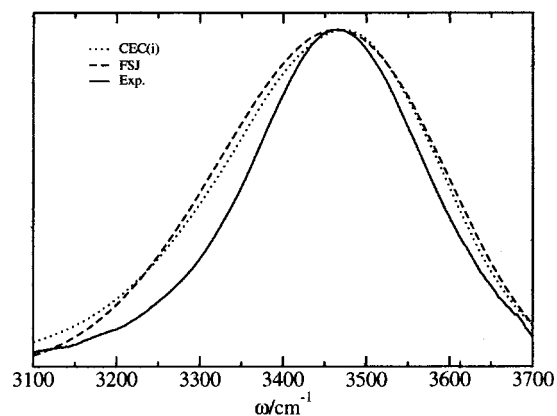


FIG. 10. Linear absorption calculated using the SLE. Dashed: CEC(i), dotted: FSJ, and solid: experiment (Ref. 19). The experimental spectrum is displaced 60  $\text{cm}^{-1}$  to the blue for a better comparison of the line shapes.

$\text{H}_2\text{O}$  (Ref. 29) and HOD in  $\text{D}_2\text{O}$  (Ref. 58) are in agreement with the trend predicted by the four-state jump model, where the observed linewidth is 23  $\text{cm}^{-1}$  broader in the blue than in the red.

Taking a slice of the two-dimensional (2D) photon-echo spectra along  $\omega_3$  for a fixed  $\omega_1$ , we observe two peaks representing stimulated emission/ground-state bleach and the excited-state absorption. We have defined the frequency difference between these peaks as the *anharmonic shift*. For  $\omega_1 = 3400 \text{ cm}^{-1}$  this shift is marked by an arrow on the photon-echo spectra in Fig. 13. The 260  $\text{cm}^{-1}$  anharmonic shift obtained in the simulation (the distance between the diagonal and the overtone peaks) is in good agreement with experiment 240 (Ref. 48) and 270  $\text{cm}^{-1}$  (Refs. 21 and 22). The calculated anharmonicity is 172  $\text{cm}^{-1}$ . The difference between the two is due to the interference between the two peaks. Only if the two peaks are well separated (i.e., the anharmonicity is much larger than the linewidth), the anharmonic shift should be equal to the actual anharmonicity.

To investigate the effect of the anharmonicity fluctuations we have carried out CEC(ii) simulations both with a fluctuating anharmonicity and by fixing it at the average value. The two, shown in Fig. 13, look very similar. However, a clear difference is observed when plotting the anharmonic shift as a function of  $\omega_1$ . When the anharmonicity is fluctuating the anharmonic shift is larger (by about 10  $\text{cm}^{-1}$ )

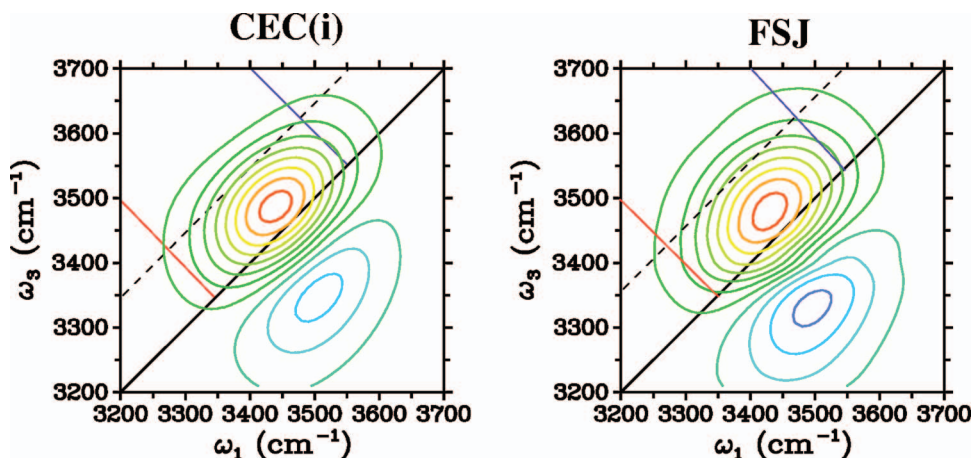


FIG. 11. (Color) Comparison of the photon-echo spectra calculated using the two SLE models. The full black line illustrates the diagonal, the dashed line is displaced 100  $\text{cm}^{-1}$  above the diagonal. The red and blue lines show where the anti-diagonal slices for Fig. 12 are taken on the red and blue sides, respectively.

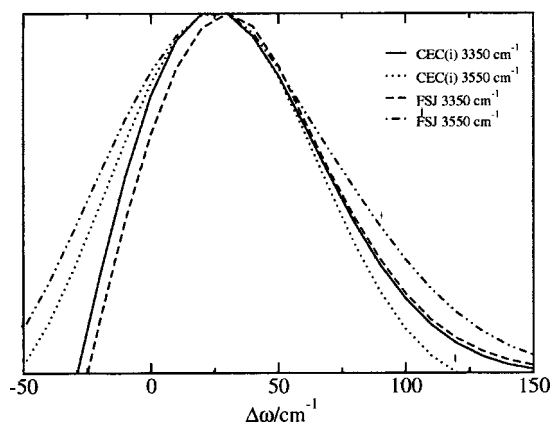


FIG. 12. Antidiagonal slices of the photon-echo spectra of Fig. 11 intersecting the diagonal. The slices are made at 3350 and 3550  $\text{cm}^{-1}$ .

for frequencies corresponding to strong hydrogen bonds ( $\omega_1 = -3300 \text{ cm}^{-1}$ ) and slightly smaller for frequencies corresponding to weak hydrogen bonds ( $\omega_1 = -3500 \text{ cm}^{-1}$ ). This is the equivalent predictions of the hydrogen-bond analysis, where the anharmonicity of the most abundant species (I) is  $176.0 \text{ cm}^{-1}$ , compared to  $164.7 \text{ cm}^{-1}$  for the more blue-shifted hydrogen-bond species II (see Table III). From this comparison it is also evident that the frequency dependence of the anharmonic shift is to a large extent determined by interference between the two peaks.

Figure 14 shows the photon-echo spectra for finite time delays  $t_2$  simulated using the CEC(ii) and the CEC(iii) methods in the impulsive limit. The peaks are spread out along the diagonal even for long time delays, suggesting a substantial inhomogeneity that is retained for longer than 1 ps. As time evolves the peaks lose their elliptical elongated shape, indicating the transition to the homogeneous regime.<sup>59,60</sup> At longer times the line shapes become more vertical and broaden in the  $\omega_3$  direction as well. This is most clearly visible in CEC(iii). The disappearance of the inhomogeneity is slower than what is experimentally observed for both the OD stretch in HOD/H<sub>2</sub>O (Refs. 29 and 30) and the OH stretch in HOD/D<sub>2</sub>O.<sup>58</sup>

We have further calculated the integrated three-pulse photon-echo signal in the impulsive limit

$$I(t_2, t_1) = \int_0^\infty dt_3 |S_I^{(3)}(t_3, t_2, t_1)|^2. \quad (13)$$

The photon-echo peak shift  $t_1^*(t_2)$  is defined as the value of  $t_1$  that maximizes  $I(t_2, t_1)$ .<sup>28,61</sup> This interesting slice of the two-dimensional signal provides a direct look at the homoge-

TABLE V. Antidiagonal linewidths for cuts through the diagonal peak in photon-echo spectrum on the red and blue sides (red and blue lines in Fig. 11). The asymmetry parameter  $\eta$  is defined in Eq. (12).

	CEC(i)	FSJ
Red side ( $3350 \text{ cm}^{-1}$ )	85.8	81.4
Blue side ( $3550 \text{ cm}^{-1}$ )	88.2	104.7
$\eta$	0.0138	0.125

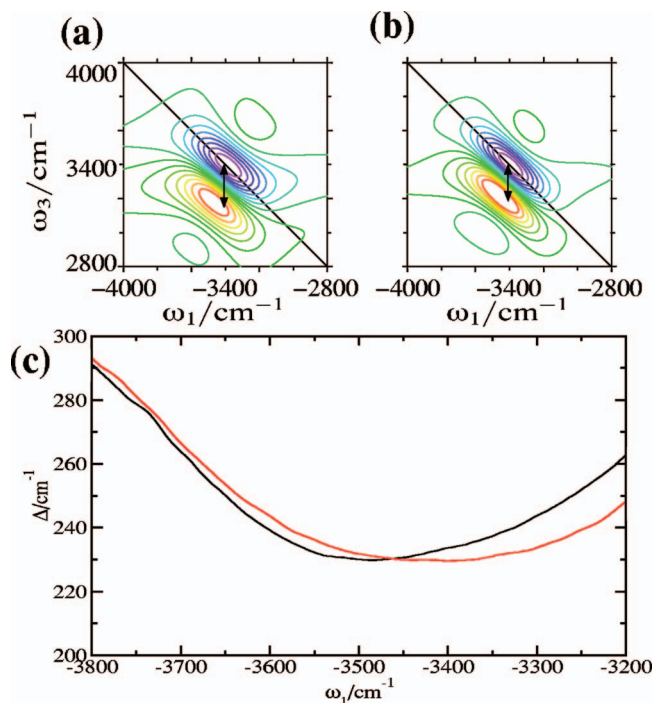


FIG. 13. (Color) Effect of the anharmonicity fluctuations. (a) CEC(ii) spectrum with fluctuating anharmonicity. (b) CEC(ii) spectrum with fixed anharmonicity. The vertical arrows indicate the anharmonic shift at  $3400 \text{ cm}^{-1}$ . (c) The anharmonic shift vs  $\omega_1$ . Black: fluctuating anharmonicity; red: fixed anharmonicity.

neous versus inhomogeneous contributions. The simulated CEC(ii) and CEC(iii) three-pulse photon-echo peak shifts are shown in Fig. 15 along with experiment<sup>19</sup> and earlier simulation (the LS3 SC model).<sup>28</sup> CEC(ii) shows a peak shift close to 34 fs for  $t_2 = 0$ , compared to 37 fs for CEC(iii) and 28 fs (experiment). Our simulations show a bump for  $t_2 = 120$  fs; the experiment has a more pronounced bump at 150 fs. The simulated decay of the peak shift versus  $t_2$  is faster than experiment. The earlier simulation<sup>28</sup> was performed using the TIP4P force field, CEC(ii), and impulsive pulses, but using the solute Hamiltonian fitted to experiment and a fixed anharmonicity. That simulation shows the same general features. However, the observed oscillation at 120 fs was more pronounced, reflecting the stronger oscillation in their frequency correlation function. No oscillation was reported in the correlation function in more recent empirical map simulations of the photon echo of the OD stretch in HOD in H<sub>2</sub>O.<sup>29,30</sup>

## VI. DISCUSSION

Photon-echo spectra of HOD in D<sub>2</sub>O were calculated using the collective electrostatic coordinate (CEC) and the four-state jump (FSJ) models for fast hydrogen-bond fluctuations. The present study assumed impulsive pulses and neglected the slow rotation and vibrational relaxation of water. These need to be included in order to simulate pump-probe experiments, where specific frequencies are probed and substantial rotational dynamics and vibrational relaxation take place during the  $t_2$  delay period. The CEC assumes Gaussian distributions of the two fluctuating collective coordinates. In the FSJ model the faster Brownian oscillator is replaced by a

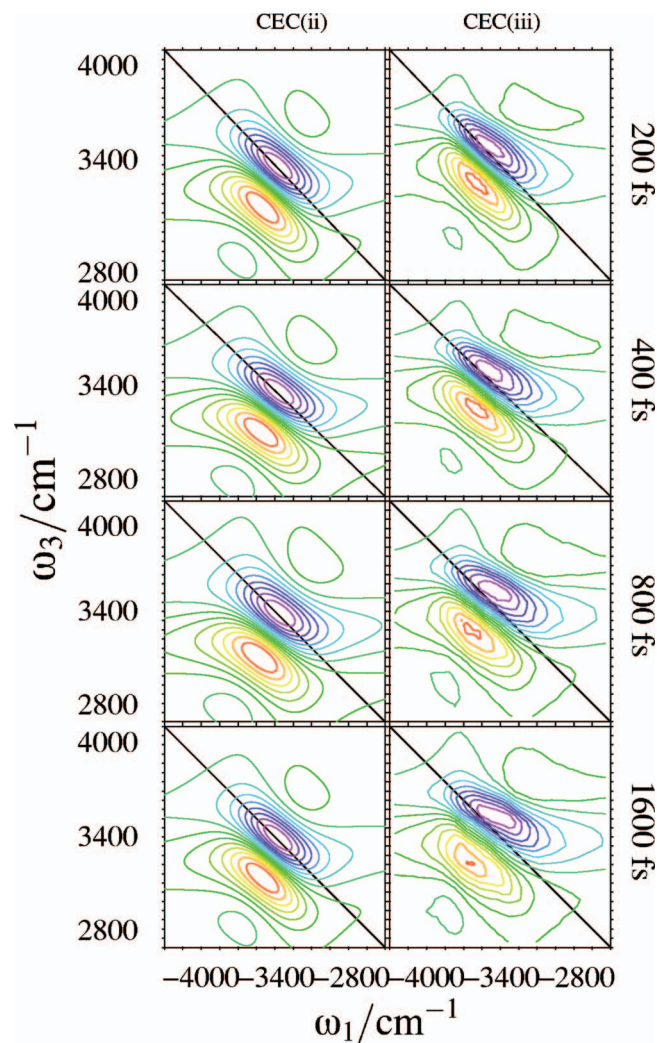


FIG. 14. (Color) Photon-echo spectra for different delay times  $t_2$  calculated using CEC(ii) and CEC(iii).

discrete kinetic model for the jumps between the four hydrogen-bonding states. The CEC model describes the hydrogen-bonding dynamics as a whereas the FSJ assumes sudden non-Gaussian jumps between the different hydrogen-bonding species, described by the kinetic equations. The FSJ hydrogen-bonding kinetics replaces the fast  $\Omega_2$  coordinate of the CEC model.

In the FSJ model, breaking a hydrogen bond on oxygen affects both the fundamental OH frequency and anharmonicity more than breaking the hydrogen bond on the hydrogen atom. Hydrogen bonding to deuterium causes a blueshift. The dependence of the anharmonicity on the electrostatic potential is built into the *ab initio* electrostatic map. We have investigated the fluctuations of the anharmonicity and found that the anharmonicity is larger when more hydrogen bonds are present and the solvent shift is larger. The anharmonicity difference between the two most abundant configurations is  $10 \text{ cm}^{-1}$ . HOD with one hydrogen bonding to H and two hydrogen bonding to oxygen has about  $10 \text{ cm}^{-1}$  larger anharmonicity than HOD with no hydrogen bonding to the H atom. This suggests that hydrogen bonding to the H atom of HOD lowered the OH stretch vibrational potential of HOD more in longer O–H bond distances, making the anharmonic-

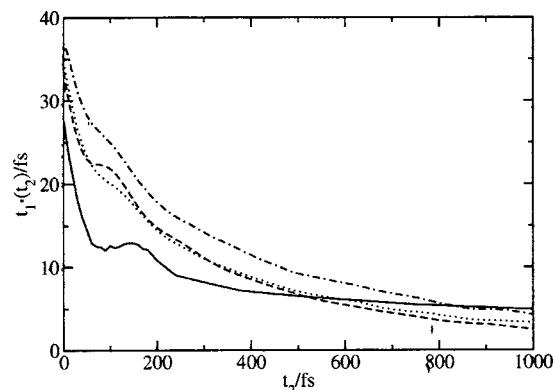


FIG. 15. Three-pulse photon-echo peak shift spectrum. Solid line: experiment (Ref. 19); dotted: CEC(ii); dot-dashed: CEC(iii); and dashed: simulated data reported in Ref. 28.

ity larger. This frequency dependence of the anharmonicity was also reported experimentally.<sup>48</sup> Anharmonicity fluctuations are also found to contribute to the three-pulse photon-echo signals. The calculation with the fluctuating anharmonicity gives about  $10 \text{ cm}^{-1}$  larger anharmonic shift defined as a frequency difference along the  $\omega_3$  axis between the peak position of the stimulated emission/ground-state bleach peak.

The triangular shape of the diagonal photon-echo peak is due to the fast femtosecond hydrogen-bonding kinetics. The FSJ model which explicitly accounts for the hydrogen-bonding kinetics reproduces this triangular shape and has a simulated  $23 \text{ cm}^{-1}$  broader linewidth in the blue than in the red, in good agreement with the  $20 \text{ cm}^{-1}$  reported from hole-burning studies.<sup>48</sup> This suggests that the non-Gaussian nature of the hydrogen-bonding dynamics is responsible for the asymmetry of the spectrum. The FSJ asymmetry parameter  $\eta$  was in better agreement with experiment than CEC(i). The overall shape of the FSJ photon-echo spectrum is in good agreement with recent experiments<sup>58</sup> while the triangular shape is less pronounced than that observed for the OD stretch in HOD/H<sub>2</sub>O.<sup>29,30</sup>

## ACKNOWLEDGMENTS

The support of the National Institutes of Health Grant No. (GM59230-005) and the National Science Foundation Grant No. (CHE-0446555) and the Air Force Office of Scientific Research (FA9550-04-1-0332) is gratefully acknowledged. We are grateful to Professor James L. Skinner for providing his simulation data and to Professor Andrei Tokmakoff for sharing his experimental photon-echo peak shift data.

<sup>1</sup>D. Eisenberg and W. Kauzmann, *The Structure and Properties of Water* (Oxford University Press, New York, 1969).

<sup>2</sup>*The Hydrogen Bond: Recent Developments in Theory and Experiments* edited by P. Schuster, G. Zundel, and C. Sandorfy (North-Holland, Amsterdam, 1976), Vols. 1–3.

<sup>3</sup>*Ultrafast Hydrogen Bonding Dynamics and Proton Transfer Processes in the Condensed Phase*, edited by T. Elsaesser and H. J. Bakker (Kluwer Academic, Dordrecht, 2002).

<sup>4</sup>G. C. Pimentel and C. H. Sederholm, *J. Chem. Phys.* **24**, 639 (1956).

<sup>5</sup>P. Wernet, D. Nordlund, U. Bergmann, *et al.*, *Science* **304**, 995 (2004).

<sup>6</sup>E. D. Isaacs, A. Shukla, P. M. Platzman, D. R. Hamann, B. Barbiellini, and C. A. Tulk, *Phys. Rev. Lett.* **82**, 600 (1999).

<sup>7</sup>A. H. Romero, P. L. Silvestrelli, and M. Parrinello, *J. Chem. Phys.* **115**,

- 115 (2001).
- <sup>8</sup>M. Bernasconi, P. L. Silvestrelli, and M. Parrinello, *Phys. Rev. Lett.* **81**, 1235 (1998).
- <sup>9</sup>A. Luzar and D. Chandler, *Nature (London)* **379**, 55 (1996).
- <sup>10</sup>S. Woutersen and H. J. Bakker, *Nature (London)* **402**, 507 (1999).
- <sup>11</sup>J. H. Guo, Y. Luo, A. Augustsson, J. E. Rubensson, C. Sathe, H. Agren, H. Siegbahn, and J. Nordgren, *Phys. Rev. Lett.* **89**, 137402 (2002).
- <sup>12</sup>R. Laenen, C. Rauscher, and A. Laubereau, *Phys. Rev. Lett.* **80**, 2622 (1998).
- <sup>13</sup>J. Stenger, D. Madsen, P. Hamm, E. T. J. Nibbering, and T. Elsaesser, *Phys. Rev. Lett.* **87**, 027401 (2001).
- <sup>14</sup>R. Rey, K. B. Møller, and J. T. Hynes, *Chem. Rev. (Washington, D.C.)* **104**, 1915 (2004).
- <sup>15</sup>C. P. Lawrence and J. L. Skinner, *J. Chem. Phys.* **117**, 5827 (2002).
- <sup>16</sup>M. L. Cowan, B. D. Bruner, N. Huse, J. R. Dwyer, B. Chugh, E. T. J. Nibbering, T. Elsaesser, and R. J. D. Miller, *Nature (London)* **434**, 199 (2002).
- <sup>17</sup>M. Falk and T. A. Ford, *Can. J. Phys.* **44**, 1699 (1966).
- <sup>18</sup>S. Yeremenko, M. S. Pshenichnikov, and D. A. Wiersma, *Chem. Phys. Lett.* **369**, 107 (2003).
- <sup>19</sup>C. J. Fecko, J. D. Eaves, J. J. Loparo, A. Tokmakoff, and P. L. Geissler, *Science* **301**, 1698 (2003).
- <sup>20</sup>W. S. Benedicht, N. Gailar, and E. K. Plyler, *J. Chem. Phys.* **24**, 1139 (1956).
- <sup>21</sup>S. Woutersen and H. J. Bakker, *Phys. Rev. Lett.* **83**, 2077 (1999).
- <sup>22</sup>H. Graener, G. Seifert, and A. Laubereau, *Phys. Rev. Lett.* **66**, 2092 (1991).
- <sup>23</sup>R. Laenen, K. Simeonidis, and A. Laubereau, *J. Phys. Chem. B* **106**, 408 (2002).
- <sup>24</sup>S. Bratos and J.-C. Leicknam, *J. Chem. Phys.* **101**, 4536 (1994).
- <sup>25</sup>A. J. Lock, S. Woutersen, and H. J. Bakker, *J. Phys. Chem. A* **105**, 1238 (2001).
- <sup>26</sup>J. Stenger, D. Madsen, P. Hamm, E. T. J. Nibbering, and T. Elsaesser, *J. Phys. Chem. A* **106**, 2341 (2002).
- <sup>27</sup>J. Stenger, D. Madsen, J. Dreyer, P. Hamm, E. T. J. Nibbering, and T. Elsaesser, *Chem. Phys. Lett.* **354**, 256 (2002).
- <sup>28</sup>A. Piryatinski, C. P. Lawrence, and J. L. Skinner, *J. Chem. Phys.* **118**, 9672 (2003).
- <sup>29</sup>J. B. Asbury, T. Steinel, C. Stromberg, S. A. Corcelli, C. P. Lawrence, J. L. Skinner, and M. D. Fayer, *J. Phys. Chem. A* **108**, 1107 (2004).
- <sup>30</sup>T. Steinel, J. B. Asbury, S. A. Corcelli, C. P. Lawrence, J. L. Skinner, and M. D. Fayer, *Chem. Phys. Lett.* **386**, 295 (2004).
- <sup>31</sup>D. W. Oxtoby, D. Levesque, and J.-J. Weis, *J. Chem. Phys.* **68**, 5528 (1978).
- <sup>32</sup>C. P. Lawrence and J. L. Skinner, *J. Chem. Phys.* **117**, 8847 (2002).
- <sup>33</sup>S. A. Corcelli, C. P. Lawrence, and J. L. Skinner, *J. Chem. Phys.* **120**, 8107 (2004).
- <sup>34</sup>K. Kwac and M. H. Cho, *J. Chem. Phys.* **119**, 2247 (2003).
- <sup>35</sup>T. Hayashi, T. I. C. Jansen, W. Zhuang, and S. Mukamel, *J. Phys. Chem. A* **109**, 64 (2005).
- <sup>36</sup>R. Kubo, *J. Math. Phys.* **4**, 174 (1963).
- <sup>37</sup>R. Kubo, *Adv. Chem. Phys.* **15**, 101 (1969).
- <sup>38</sup>D. Gamliel and H. Levanon, *Stochastic Processes in Magnetic Resonance* (World Scientific, River Edge, NJ, 1995).
- <sup>39</sup>J. H. Freed, G. V. Bruno, and C. F. Polnaszek, *J. Phys. Chem.* **75**, 3385 (1971).
- <sup>40</sup>R. Rey and J. T. Hynes, *J. Chem. Phys.* **104**, 2356 (1996).
- <sup>41</sup>A. Piryatinski, C. P. Lawrence, and J. L. Skinner, *J. Chem. Phys.* **118**, 9664 (2003).
- <sup>42</sup>C. P. Lawrence and J. L. Skinner, *Chem. Phys. Lett.* **369**, 472 (2003).
- <sup>43</sup>K. Kwac, H. Lee, and M. Cho, *J. Chem. Phys.* **120**, 1477 (2004).
- <sup>44</sup>M. J. Frisch, G. W. Trucks, H. B. Schlegel *et al.*, GAUSSIAN03, Revision B.05, Gaussian Inc., Pittsburgh, PA, 2003.
- <sup>45</sup>H. J. C. Berendsen, D. van der Spoel, and R. van Drunen, *Comput. Phys. Commun.* **91**, 43 (1995).
- <sup>46</sup>H. J. C. Berendsen, J. P. M. Postma, W. F. v. Gunsteren, A. DiNola, and J. R. Haak, *J. Chem. Phys.* **81**, 3684 (1984).
- <sup>47</sup>S. Mukamel, *Principles of Nonlinear Optical Spectroscopy* (Oxford University Press, New York, 1995).
- <sup>48</sup>R. Laenen, C. Rauscher, and A. Laubereau, *J. Phys. Chem. B* **102**, 9304 (1998).
- <sup>49</sup>T. I. C. Jansen, W. Zhuang, and S. Mukamel, *J. Chem. Phys.* **121**, 10577 (2004).
- <sup>50</sup>M. Diraison, Y. Guissani, J.-C. Leicknam, and S. Bratos, *Chem. Phys. Lett.* **258**, 348 (1996).
- <sup>51</sup>S. Mukamel, *Phys. Rev. A* **28**, 3480 (1983).
- <sup>52</sup>S. Mukamel and D. Abramavicius, *Chem. Rev. (Washington, D.C.)* **104**, 2073 (2004).
- <sup>53</sup>C. P. Lawrence and J. L. Skinner, *J. Chem. Phys.* **118**, 264 (2003).
- <sup>54</sup>F. Csajka and D. Chandler, *J. Chem. Phys.* **109**, 1125 (1998).
- <sup>55</sup>K. B. Møller, R. Rey, and J. T. Hynes, *J. Phys. Chem. A* **108**, 1275 (2004).
- <sup>56</sup>A. M. Moran, J. Dreyer, and S. Mukamel, *J. Chem. Phys.* **118**, 1347 (2003).
- <sup>57</sup>J. B. Asbury, T. Steinel, K. Kwac, S. A. Corcelli, C. P. Lawrence, J. L. Skinner, and M. D. Fayer, *J. Chem. Phys.* **121**, 12431 (2004).
- <sup>58</sup>J. D. Eaves, J. J. Loparo, C. J. Fecko, S. T. Roberts, A. Tokmakoff, and P. L. Geissler, *Proc. Natl. Acad. Sci. U.S.A.* (in press).
- <sup>59</sup>K. Okumura, A. Tokmakoff, and Y. Tanimura, *Chem. Phys. Lett.* **314**, 488 (1999).
- <sup>60</sup>Y. Tanimura and S. Mukamel, *J. Chem. Phys.* **99**, 9496 (1993).
- <sup>61</sup>M. Cho, J.-Y. Yu, T. Joo, Y. Nagasawa, S. A. Passino, and G. R. Fleming, *J. Phys. Chem.* **100**, 11944 (1996).